Materials Horizons

ROYAL SOCIETY OF CHEMISTRY

COMMUNICATION

View Article Online
View Journal | View Issue

Cite this: *Mater. Horiz.*, 2025, **12**, 520

Received 18th September 2024,
Accepted 24th October 2024

DOI: 10.1039/d4mh01291g

rsc.li/materials-horizons

Spider-silk inspired ultrafast alkali-induced molecular aggregation for 3D printing arbitrary tubular hydrogels†

Yang Lyu,[a] Zhongying Ji,*[ab] Di Liu,[c] Xinqiang Xu,[d] Rui Guo,[ab] Xinyan Shi[c] and Xiaolong Wang *[ab]

Fabricating tubular hydrogel models with arbitrary structural complexity and controllable diameters using an ultrafast, facile yet universal method is desirable for vascular prototypes yet still a great challenge. Herein, inspired by the denaturing ability of spider silks, a novel strategy to induce complexation *via* applying highly concentrated alkali into a polyvinyl alcohol/ionic liquid (PVA/IL) solution, *i.e.*, alkali-induced molecular aggregation (AMA), is proposed to achieve such purpose. This strategy enables the rapid and facile fabrication of tubular hydrogel architectures with tunable diameters, controllable thicknesses, and excellent mechanical performance with a tensile strength of up to 1.1 MPa and stretchability exceeding 600%. Importantly, this novel strategy combined with 3D printing facilitates the rapid fabrication of a variety of precise tubular hydrogel models with connected cavity structures which are difficult to achieve using current methods. This ultrafast solidification strategy could also be extended to various alkalis, cations and anions to build different hydrogels, showcasing its versatility and universality. Hence, this strategy can be pioneering to rapidly fabricate complex three-dimensional and hollow enclosed hydrogel models for simulating endovascular interventional therapy.

New concepts

Here, inspired by spider dragline silk, we introduce an innovative concept known as "alkali-induced molecular aggregation (AMA)" to rapidly fabricate tubular hydrogels. By leveraging this novel approach, a 3D printed hydrogel-based vascular model was designed based on the unique reaction mechanism and molecular diffusion direction. The transition from fluid to solid occurs instantaneously (in less than 0.5 ns) by introducing an alkaline solution (the concentration of OH^- is at least 0.1 mol L^{-1}) to a mixture solution of PVA and $[BMIM]BF_4$. The interaction between these components results in a distinct phase transition, with a clear molecular diffusion direction, always moving from the alkali towards PVA/$[BMIM]BF_4$. This unique diffusion directionality assisted extrusion-based 3D printing can easily fabricate vascular-like cavity structures. Compared with other reported methods, this alkali-induced complexation permits the simple, rapid and reliable fabrication of hydrogel-based vascular-like cavity structures with tunable shapes and thicknesses. The interconnected tubular hydrogel models exhibit strong structural integrity, spacious chamber size, and customizable mechanical properties, making them ideal for vascular intervention training. Using this approach, we successfully created a variety of vascular models, including an intrapulmonary vascular model with a complex vascular network, a feat that is challenging to achieve with traditional materials and 3D printing techniques.

1. Introduction

In nature, organisms have evolved a variety of unique functions and survival skills that inspire the design and synthesis of functional materials, mimicking nature.[1–4] Over the past two decades, various processing techniques such as melt-drawing, microfluidic methods, and electrospinning have been developed to fabricate high-performing materials, drawing inspiration from spider dragline silk.[5–7] However, a few studies mentioned spider silk's ability to denature, which is converted from liquid to solid, triggered by external stimuli. This unique property allows spiders to efficiently create solid fibers from liquid polymer solutions stored within their bodies, a process far more energy efficient than traditional methods using thermoplastic polymers in modern industry.[8] Research suggests

[a] *Shandong Laboratory of Advanced Materials and Green Manufacturing at Yantai, Yantai Zhongke Research Institute of Advanced Materials and Green Chemical Engineering, Yantai, 264006, China*
[b] *State Key Laboratory of Solid Lubrication, Lanzhou Institute of Chemical Physics, Chinese Academy of Sciences, Lanzhou 730000, China. E-mail: jizy@licp.cas.cn, wangxl@licp.cas.cn*
[c] *Key Laboratory of Rubber-plastics, Ministry of Education, School of Polymer Science and Engineering, Qingdao University of Science & Technology, Qingdao, 266042, China*
[d] *School of Chemistry and Chemical Engineering, Key Laboratory of Materials-Oriented Chemical Engineering of Xinjiang Uygur Autonomous Region, Shihezi University, Shihezi, 832003, China*

† Electronic supplementary information (ESI) available. See DOI: https://doi.org/10.1039/d4mh01291g

that spiders can regulate this phase transition by controlling the pH and ion concentration in the processing environment.[9,10] This special solidification does not occur by the common mechanisms of heat transfer or chemical crosslinking, and a phase transition is facilitated by the formation of intermolecular hydrogen bonds. Subsequently, spider silk obtains a stable structure through inter-protein interactions and crystallization. The transition between fluid and solid states remains a challenging problem in condensed matter physics.[11,12] A common strategy for the transition requires ambient pressure and temperature and rheological properties of materials, and it is unable to construct complex shapes rapidly like spider dragline silk. In particular, due to difficult-to-control phase transition, the rapid and reliable fabrication of materials with complex macroscopic structures remains challenging.

Tubular structures serve as important conduits for transporting matter in nature, such as the blood vessels of animals and the stalks of herbaceous plants. Recent works have intensively explored tubular structures and have demonstrated their many unique and attractive characteristics. He *et al.* designed and constructed soft tubular actuators using a liquid crystal elastomer that can be easily patterned with programmable strain.[13] Yang *et al.* reported a bioinspired phototropic MXene-reinforced soft tubular actuator that exhibits omnidirectional self-orienting ability. The distinct hollow structure could endow the MXene-LCE soft tubular actuators with fast photoresponsive characteristics and excellent photothermal controllability through retarding the heat conduction along the radial direction.[14] The fabrication of tubular hydrogel architectures has garnered significant interest due to their applications in tissue engineering, chemical actuators, medicine transportation, separation, and microfluidics. These hydrogels are valued for their high water content, biocompatibility, softness and flexibility.[15,16] However, creating hollow hydrogels with intricate structures remains challenging due to the lack of robust and convenient methods for production and dimensional control. Currently, three major methods have been proposed for the construction of 3D hollow tubules: (1) subtractive manufacturing by carving to fabricate millimeter-scaled vascular scaffolds[17]; (2) precise knitting of fasciculus to construct micro-scaled artificial tubules[18]; and (3) additive manufacturing by 3D printing to print millimeter-scaled tubules.[19] However, owing to the limited accuracy of these methods, the fabrication of tubules smaller than 600 μm in diameter remains a challenge. In addition, hollow structures are not completely remodeled with these methods, and the complicated fabricating procedures are extremely difficult to control. Therefore, fabricating tubular hydrogels precisely is crucial and difficult.[20–22] However, the embedded 3D printing strategy has gained increasing popularity for resolving the abovementioned issues.[23–27] A suspension medium is used to support the deposition of reactive inks in 3D space before crosslinking and then solidification through ultraviolet light by raising the temperature.[28–31] As examples of this strategy, Bhattacharjee and co-workers used hydrogels and living cells to print complex 3D objects, thin closed shells, and hierarchically branched tubular networks.[32] However, the precision and level of detail depend tightly on various parameters including the rheology of inks and the medium. Additionally, the shape of 3D printed objects may be influenced by surface tension and gravity during the crosslinking process.[33] Our previous research has shown that tubular hydrogels with internal channels and cavity structures could be prepared *via* metal ion-induced interface supramolecular assembly of hydrogel layers on thermally splitting templates, yet many drawbacks remain including a complex preparation process, low accuracy and long production times.[34] Therefore, the development of a biomimicking vascular model that not only replicates organ shapes and internal cavities but also simplifies fabrication remains a significant challenge. Here, inspired by spider dragline silk, we introduce an innovative strategy known as alkali-induced molecular aggregation (AMA) to rapidly fabricate tubular hydrogels. By leveraging this novel approach, a 3D printed hydrogel-based vascular model was designed based on the unique reaction mechanism and molecular diffusion direction. Our previous research demonstrated a rapid and innovative process for creating polyvinyl alcohol (PVA) hydrogels induced by 1-butyl-3-methylimidazolium tetrafluoroborate ([BMIM]BF_4) and NaOH.[35] The transition from fluid to solid occurs instantaneously (in less than 0.5 ns) by introducing an alkaline solution (the concentration of OH^- is at least 0.1 mol L^{-1}) to a mixture solution of PVA and [BMIM]BF_4. The interaction between these components results in a distinct phase transition, with a clear molecular diffusion direction, always moving from the alkali towards PVA/[BMIM]BF_4. This unique diffusion directionality assisted extrusion-based 3D printing can easily fabricate vascular-like cavity structures. Compared with other reported methods, this alkali-induced complexation permits the simple, rapid and reliable fabrication of hydrogel-based vascular-like cavity structures with tunable shapes and thicknesses. The interconnected tubular hydrogel models exhibit strong structural integrity, spacious chamber size, and customizable mechanical properties, making them ideal for vascular intervention training. Using this approach, we successfully created a variety of vascular models, including an intrapulmonary vascular model with a complex vascular network, a feat that is challenging to achieve with traditional materials and 3D printing techniques.

2. Results and discussion

2.1 AMA strategy inspired by the rapid solidification of spider silk

The design of rapid solidification in a water solution was inspired by the ability to create solid fibers from the liquid silk of spiders which has been infrequently mentioned in previous research. The formation process of silk is a highly efficient processing strategy in the natural world. A phase transition occurs solely under flow in an aqueous solution, without controlled processing conditions such as temperature and

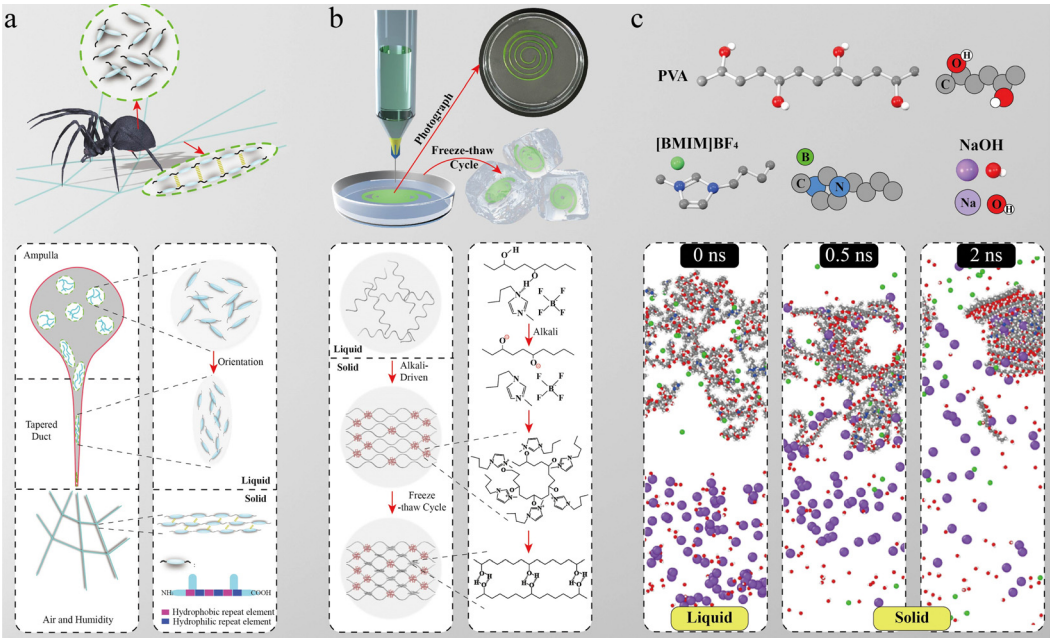

Fig. 1 Schematic illustration of fabricating hollow hydrogel architectures inspired by the rapid solidification process of spider's silk production. (a) Conversion process of the silk from a liquid phase to a solid phase through the disruption of the hydration layer and intermolecular hydrogen bonds. (b) Bioinspired fabrication strategy taking advantage of complexation and crystallization to enable a phase transition from liquid to solid in PVA/ionic liquids within a water solution (using PVA/[BMIM]BF_4 as a model system). (c) Molecular dynamics demonstrate that the phase transition induced by alkali occurs within 0.5 ns once the two solutions are mixed.

pressure (Fig. 1a). The specific work required is several orders of magnitude smaller than that of commercial molding methods. To date, few material systems have been reported that can reproduce this mechanism under ambient conditions.[36–39] In this study, we developed a system similar to spider silk to create hydrogels from an aqueous solution (PVA–OH hydrogel). Similar to the flow-induced crystallization of spider silk, the alkali-induced complexation was employed to solidify the hydrogel rapidly. In this process, the hydroxyl groups of PVA chains were deprotonated *via* alkali induction; meanwhile, the complexation instantaneously occurred between O^- and cations in ILs. Additionally, the mechanical properties of the hydrogels were further enhanced by the dense hydrogen bond networks created during freeze–thaw cycles (Fig. 1b). Molecular dynamic (MD) simulations showed that the phase transition in our system occurs within 0.5 ns, similar to the process of forming spider silks. More importantly, two solutions follow clear molecular diffusion direction, that is always diffusing from alkali to PVA/ILs (Fig. 1c). This special diffusion directionality assisted extrusion-based 3D printing can easily fabricate cavity structures and provide more potential to simply and rapidly fabricate hydrogel-based freeform tubular models (Movie S1, ESI†).

2.2 Fabrication of PVA–OH hydrogel films based on the universal AMA strategy

In the preparation process, a strong alkaline hydroxide was introduced into PVA/ILs, resulting in two sequential events. Initially, the OH^- ions from the alkaline hydroxide attacked the hydroxyl groups of PVA, leading to the deprotonation of the hydroxyl groups within the PVA chains. Subsequently, the newly formed O^- groups in PVA interacted with free cations to immediately form a complex. This complexation process restricted the movement of polymer chains, thereby forming the initial networks of hydrogels. Following this, the freeze–thaw process facilitated PVA crystallization, resulting in the formation of additional networks. The interaction between the hydroxyl groups in PVA and the OH^- moieties of the highly concentrated NaOH solution led to an acid–base reaction [eqn (1)], as previously confirmed by existing literature research.[40,41] The chemical structure evolution of PVA–OH hydrogels was analyzed using Fourier transform infrared (FTIR) spectroscopy and solid-state nuclear magnetic resonance spectroscopy (ssNMR) to elucidate the complexation process. As shown in Fig. 2a, the appearance and sharpness of the peak at 1142 cm^{-1} for PVA–OH hydrogels confirmed the reorganization of the polymer chains after the reaction with NaOH and cations. Moreover, the intensity of the peak attributed to the CH_2 wagging and twisting at 1018 cm^{-1} decreased gradually with an increase in the alkali concentration. This suggests that the C–H bonds of CH_2 groups of the backbone are less free to deform out of the plane, which indicates that the polymer chains are more confined to the free deformation of the C–H bonds mainly owing to the complexation. The NaOH attack leads to the hydrolysis of the ester group of the acetate moieties from the polymer backbone as confirmed by ssNMR spectroscopy, and the ^1H signal of the acetate methyl group proton signals disappeared[42] (Fig. 2b). Based on this

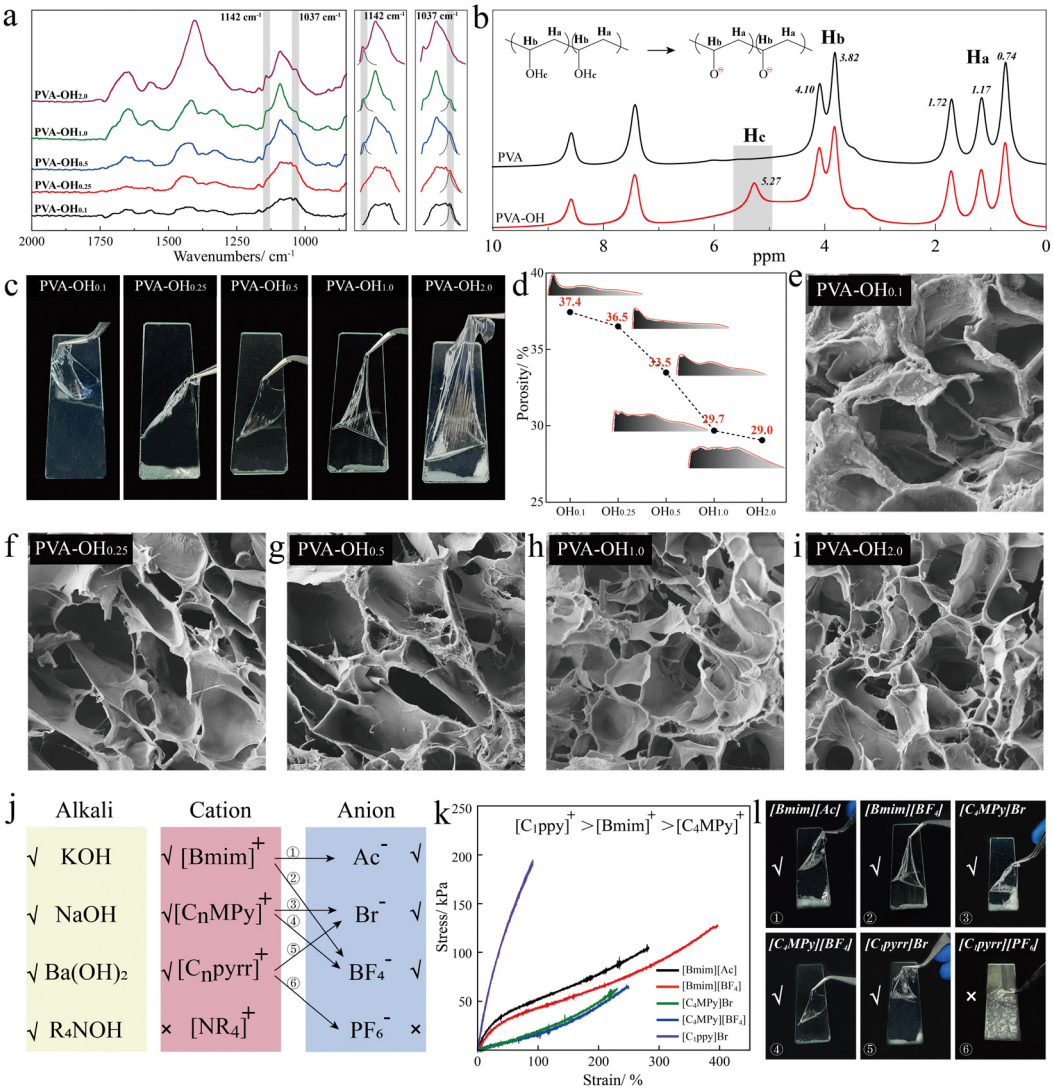

Fig. 2 Characterization and formation mechanism. (a) FTIR spectra of PVA–OH hydrogels induced by different alkalinities. (b) ssNMR spectra of PVA and PVA–$OH_{2.0}$. (c) Photographs of PVA–OH hydrogels induced by different alkalinities. (d) Calculated porosity of different PVA–OH hydrogels calculated based on SEM images. (e)–(i) SEM images of PVA–OH hydrogels with the alkalinity from 0.1 to 2.0. (j) Universality of the alkali-induced strategy; the tick indicates that the strategy for preparing PVA–OH hydrogels is feasible. (k) Stress–strain curves of PVA–OH hydrogels with different ionic liquids under the alkalinity of 2.0 mol L^{-1}. (l) Expanding a variety of ILs to fabricate PVA–OH hydrogels to evaluate the universality of this strategy.

mechanism, a hydrogel membrane can be easily obtained by immersing the PVA/[BMIM]BF_4 solution in a NaOH solution (Fig. 2c). This method of rapid manufacturing requires an alkali concentration over 0.1 mol L^{-1}. By increasing the alkalinity, a more intact morphology and higher mechanical strength of the hydrogel membrane can be achieved (Fig. 2d). The density of crosslinking networks in PVA–OH hydrogels is positively correlated with the concentration of alkali, as evidenced by the calculation of porosity from cross-sectional SEM images. SEM images further illustrate this point, showing gradual densification of the hydrogel networks with an increased alkali content (Fig. 2e–i and Fig. S1, ESI†). To assess the generalizability of this approach, we tested it with various alkalis and different types of ionic liquids (Fig. 2j). Our findings indicate that the concentration of alkali is the key factor in complex formation, rather than the specific type of alkali. Any alkali with a concentration exceeding 0.1 mol L^{-1} can potentially induce complexation. When it comes to ionic liquids, those with highly water-soluble anions and cations are more likely to form complexes (Fig. 2k. The structural formula of cations is shown in Fig. S2, ESI†). Cations are the main factors determining the mechanical properties of PVA–OH hydrogels ($[C_1ppy]^+ > [BMIM]^+ > [C_4MPy]^+$). In addition, we experimentally found that the kinds of cations have a great impact on the strength of hydrogels. As electron acceptors in complexation, the ability to accept electrons of cations directly determine the density of complexation networks ($[C_1ppy]^+ > [BMIM]^+ > [C_4MPy]^+$). The hydrogel membranes fabricated by different ionic liquids are depicted in Fig. 2l. Notably, these membranes exhibit adjustable thickness, mechanical strength

and stretchability by varying the alkali-induced time and concentration. These findings highlight the rapid fabrication of hydrogels using various alkalis and ionic liquids through this strategy.

$$R\text{–}OH + Na^{+}OH^{-} \rightleftharpoons R\text{–}O^{-}Na^{+} + H_2O \quad (1)$$

2.3 Mechanical properties of PVA–OH hydrogels induced by alkalinity

The impacts of NaOH concentration and freeze–thaw cycles on the mechanical properties of PVA–OH hydrogels are shown in Fig. 3a–e. Crosslinking PVA–OH hydrogels with NaOH solutions ranging from 0.1 to 2.0 mol L^{-1} resulted in successful gelation. Fig. 3a indicates that all samples displayed elastic behavior up to 100% strain and exhibited excellent ductility, stretching beyond 300% of their original length (only complexation). PVA–$OH_{2.0}$ exhibited superior mechanical strength with ultimate strengths exceeding 0.2 MPa and elastic moduli above 2.2 MPa. Freeze–thaw cycles led to denser PVA chains, gradually increasing their elastic modulus and mechanical strength (Fig. 3b. Detailed images are shown in Fig. S3, ESI†). The combined effects of complexation and crystallization further enhanced the strength of PVA–OH hydrogels, which reached ultimate strengths above 1.1 MPa and elastic moduli above 3.6 MPa. Adjusting the NaOH concentration and crystallinity resulted in three orders of magnitude change in the strength of PVA–OH hydrogels, ranging from 0.02 to 1.1 MPa (Fig. 3c).

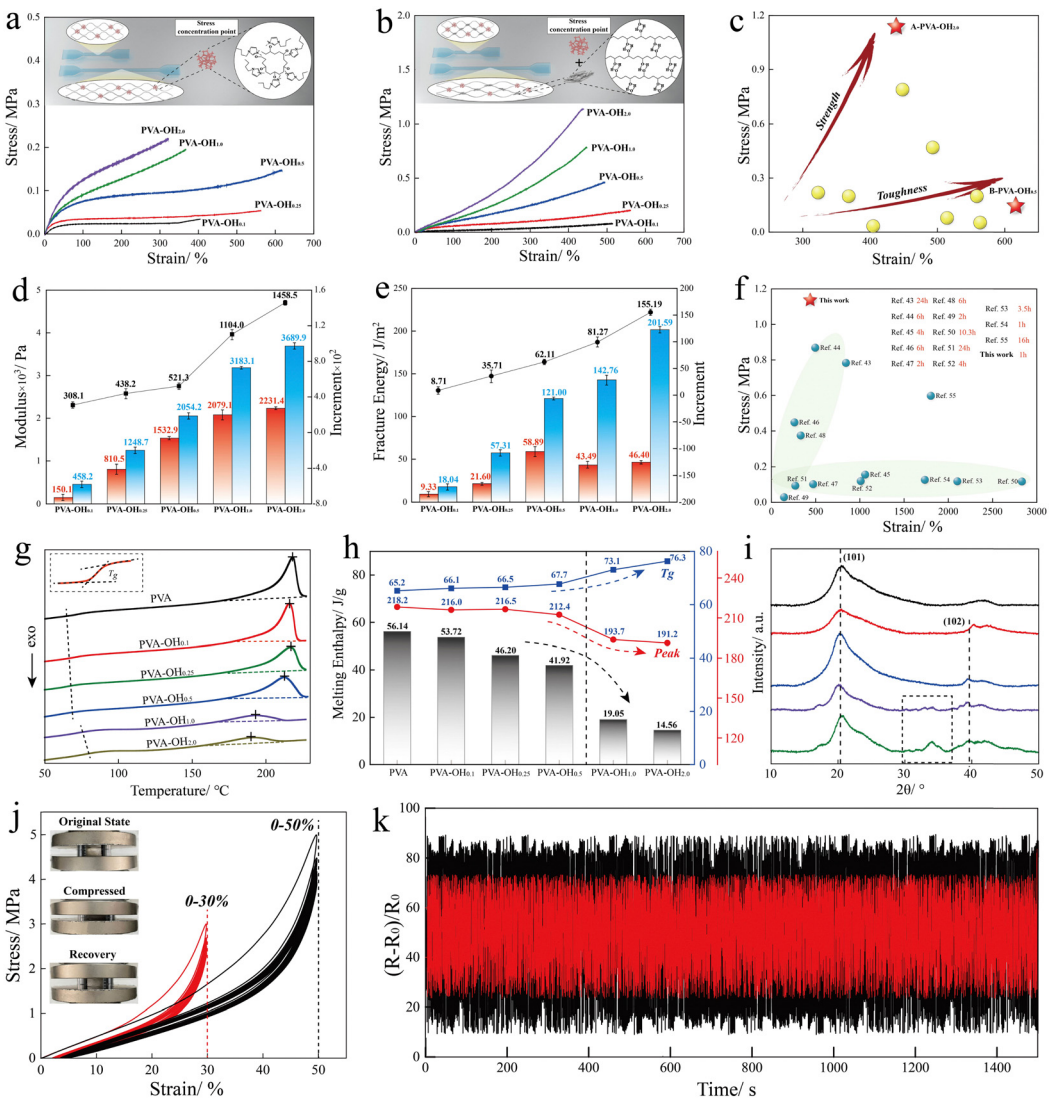

Fig. 3 Mechanical, thermal, and electrical properties of PVA–OH hydrogels. Stress–strain curves of PVA–OH hydrogels made with different alkalinities (a) without freeze–thaw cycles and (b) with freeze–thaw cycles. (c) Comparison of the mechanical properties of hydrogels with and without freeze–thaw cycles. Comparison of the (d) modulus and (e) fracture energy of hydrogels made with different alkalinities. (f) Ashby charts of the mechanical properties and time-spending of PVA–OH hydrogels *versus* various other PVA-based hydrogels. (g) DSC curves and (h) specific parameters of PVA–OH hydrogels made with different alkalinities with freeze–thaw cycles. (i) X-ray diffraction curves of PVA–OH hydrogels with freeze–thaw cycles. (j) Cyclic compressive stress–strain curves for PVA–OH hydrogels and (k) the changes of electrical signals in the process.

Both modulus and fracture energy increased significantly with freeze–thaw cycles, and a sharp increase appeared when the NaOH concentration exceeded 1 mol L^{-1} (Fig. 3d and e). It demonstrated that strong alkali media ($c(OH^-) > 1$ mol L^{-1}) can efficiently deprotonate PVA to form a strong binding ligand. Additionally, the Ashby chart in Fig. 3 provides a visual comparison of the mechanical properties and preparation time of PVA–OH hydrogels with other PVA-based hydrogels documented in the existing literature.[43–55] The study demonstrates that the preparation time of PVA–OH hydrogels is notably short compared to the existing PVA-based hydrogels, while exhibiting superior mechanical properties (Fig. 3f). The decrease in crystallinity was further confirmed by differential scanning calorimetry (DSC) to observe the PVA crystalline behavior influenced by complexation (Fig. 3g and h). Strong complexation hinders PVA chains' free mobility, which restricts the formation of crystals with the formal freeze–thaw method. Furthermore, the glass transition temperature (T_g) increased at 1 mol L^{-1} NaOH concentration due to the complexation hindering polymer chain motion. X-ray diffraction measurements (Fig. 3i) revealed distinct diffraction peaks at approximately $2\theta = 20^\circ$ and $2\theta = 41^\circ$, corresponding to the (101) and (102) diffraction reflection planes, respectively. The compressibility and self-recovery properties were assessed using a cylindrical specimen ($PVA–OH_{2.0}$) subjected to varying strains, with compressive stress values of approximately 2.9 MPa at 30% strain and 5.0 MPa at 50% strain, without any observed fractures (Fig. 3j). Furthermore, the stability of the electrical signal was evaluated by monitoring resistance changes during cyclic compressive tests, showing a consistent relative resistance ($\Delta R/R_0$) of 50 over 1500 s (500 cycles) without significant degradation (Fig. 3k). Additional electrical characterization methods are presented in Fig. S4 (ESI†).

2.4 Construction of arbitrary and complex 3D tubular hydrogel architectures

Writing 3D structures in a medium is an effective method for creating intricate 3D objects, thin closed shells and hierarchically branched tubular networks. This approach allows for the creation of suspended structures with diverse designs by overcoming surface tension, gravity and particle diffusion.[56,57] However, different from common direct writing 3D printing, the rapid solidification of the materials is essential to trip and hold the injected material behind the moving needle. It is a great challenge for the rheological properties of the medium and injected materials, as well as their rapid solidification ability. To address this challenge, cellulose nanofibers (CNF) were incorporated into both the injected material (NaOH solution) and the medium (PVA/[BMIM]BF_4) to optimize the rheological properties (Fig. S5, ESI†). A microscale capillary tip sweeps out a complex pattern as NaOH/CNF is injected into the PVA/[BMIM]BF4/CNF gel medium. Complex objects can be generated because the drawn structure can solidify rapidly and generate support on its own. As shown in Fig. 4a, the modulus increased by four orders of magnitude as long as mixing PVA/[BMIM]BF_4/CNF (①) and NaOH/CNF (②), demonstrating excellent rapid solidification ability. The injected NaOH/CNF samples displayed shear thinning behavior, with viscosities gradually increasing with a higher CNF content (Fig. 4b). All injected materials were conducted using a 2 mol L^{-1} NaOH solution and 1 wt% CNF unless specified otherwise. The process of 3D printing is shown in Fig. 4c, and 3D structures are made by carefully tracing out a series of pre-programmed paths within a medium using a microneedle. Benefiting from the diffusion direction, NaOH/CNF diffuses into PVA/[BMIM]BF_4/CNF after being injected from the needle and leaves a cavity in its original position. This unique approach distinguishes itself from others by directly producing 3D vascular structures instead of closed shells (Fig. 4d). Rheological analysis under shear mode demonstrated that NaOH/CNF can be fluidized at low shear stress (5.37 Pa), allowing for precise control over structure formation with minimal pressure drop (Fig. 4e). The flow behavior of the injected material within the medium adheres to an ideal volume-conserving relationship ($Q = \frac{1}{4}\pi abv$, where Q is the flow rate and v is the needle speed, Fig. S6, ESI†). Different needle diameters can be corrected by a correction factor (k) to establish a positive correlation between Q and $\frac{1}{4}\pi abv$ (shadow in Fig. 4f. The data samples are from four needles with different diameters, 0.21, 0.34, 0.41 and 0.51 mm, Fig. S7, ESI†). Fig. 4g shows that the hydrogel tubes with different diameters can be easily fabricated by the above strategy. The diameter of hydrogel tubes is slightly larger than that of needles due to the diffusion reaction and extrusion swell. According to our research, the diameter of hydrogel tubes is influenced by four parameters, the diameter of the needle, drop pressure, 3D printing speed and NaOH concentration. The hydrogel tubes with diameters from 200 to 2900 μm can be fabricated by adjusting those parameters (Fig. 4h). Small diameter hydrogel tubes require delicate structure control and low-density complexation, yet accompanying relatively high surface roughness of tubes (Fig. 4i–l). A hollow hydrogel structure with the shape of pulmonary vessels and a spiral tube with a large aspect ratio ($L/D = 41.2$) was fabricated by this strategy (Fig. 4m and n). By adjusting the concentration of CNF in the medium and the number of freeze–thaw cycles, we were able to produce highly transparent models. For instance, a vascular model was printed using a medium containing 0.5 wt% CNF and subjected to a single freeze–thaw cycle lasting for 2 hours, resulting in the structures depicted in Fig. 4o and p (additional images of 3D hollow hydrogel structures can be found in Fig. S8, ESI†). Furthermore, we present two molding techniques to address the challenges associated with manufacturing ultra-thin hydrogel membranes (doctor-blade method, Fig. S9 and Movie S2, ESI†) and intricate hydrogel structures (template method, Fig. S10, ESI†) based on the same methodology.

2.5 Vascular hydrogel structures used for simulation of biomedical practices

Endovascular interventional therapy is widely recognized as the most effective approach for treating endovascular lesions. Vascular hydrogel models have emerged as indispensable tools for training in realistic simulations of endovascular

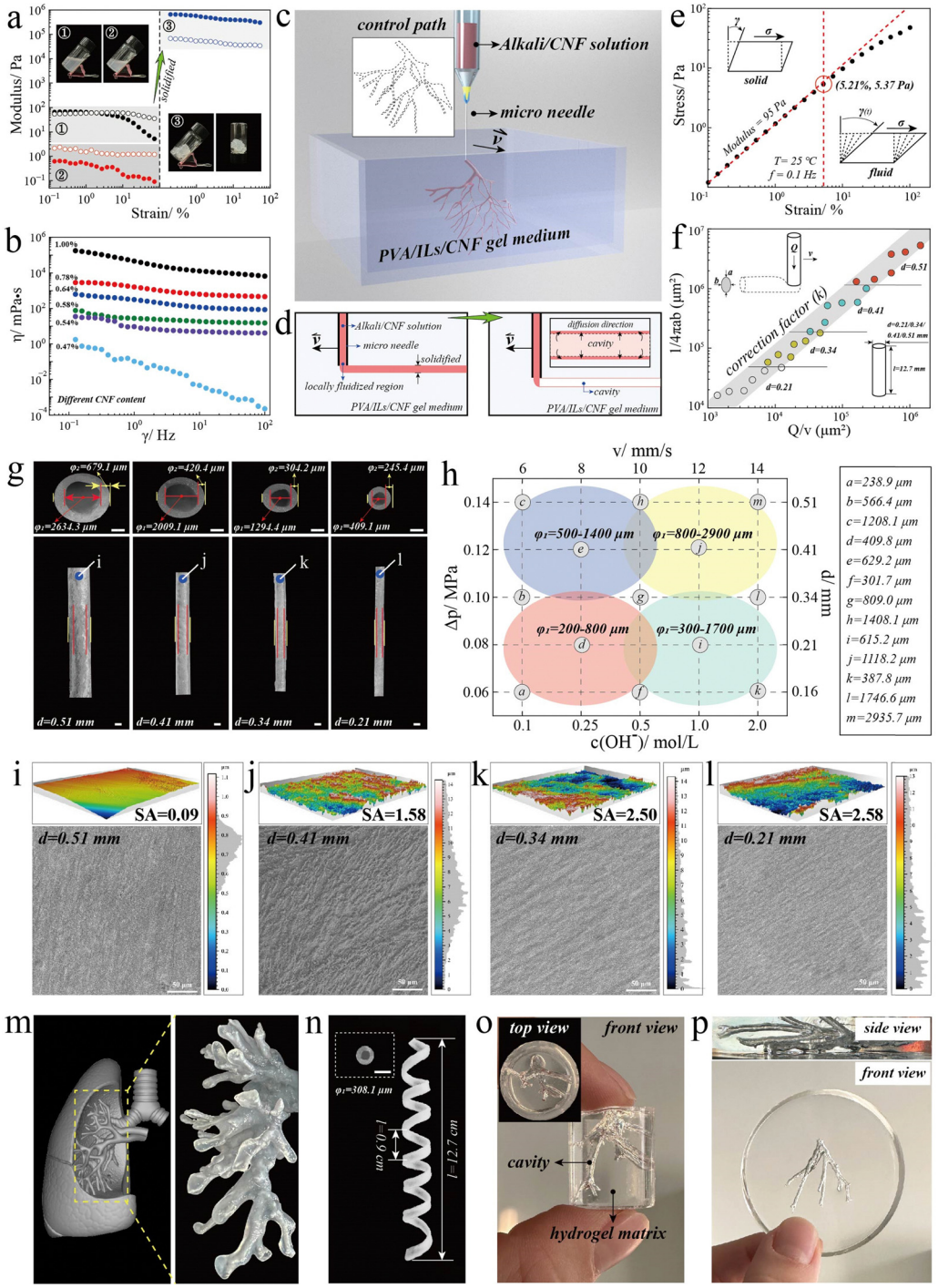

Fig. 4 Stable writing in medium and the prepared hollow hydrogel structures and objects. (a) Rheological properties of NaOH/CNF, PVA/[BMIM]BF_4/CNF and the hydrogel. The solid and hollow circles represent the storage (G') and loss modulus (G''), respectively. ①, ② and ③ represent PVA/[BMIM]BF_4/CNF, NaOH/CNF and the solidified hydrogel (PVA–$OH_{2.0}$), respectively. (b) The viscosity curves of different CNF contents in NaOH solution. (c) The schematic illustration of fabricating hollow hydrogel architectures by 3D printing. Both extrudate and medium are mixed with CNF to adjust the rheological properties (Movie S3, ESI†). (d) Mechanism of formation of the tubular hydrogel during the 3D printing process. (e) NaOH/CNF gel is a yield stress material, which elastically deforms at low shear strains and fluidizes at high strains. Stress–strain measurements reveal a shear modulus of 95 Pa and a yield stress of 5.37 Pa. (f) The cross-sectional area of written features exhibits nearly ideal behavior over a wide range of tip speeds (v) and flow rates (Q). The trend line corresponds to the volume conserving relationship, $Q = \frac{1}{4}\pi abv$. (g) The hydrogel tubes fabricated by 3D printing with different needle diameters, including main views (below photos), cross-sectional views (above photos) and actual diameters (in cross-sectional views). (h) Four important parameters that depend on the tube diameters of hydrogels, including alkali concentration ($c(OH^-)$, below abscissa), needle diameters (d, right vertical), printing speed (v, top abscissa) and pressure drop (Δp, left vertical). Values on the right are specific diameters of hydrogel tubes from 200 to 2900 μm adjusted by the four parameters. (i)–(l) The surface morphology images and roughness of the hydrogel tubes corresponding to Fig. 4g, respectively. (m) A hollow hydrogel structure with the shape of pulmonary vessels. (n) A 3D printing hydrogel spiral tube with a diameter of 308.1 μm and a length of 12.7 cm. (o) and (p) A 3D printing vascular structure in the hydrogel matrix to prepare a highly transparent vascular model.

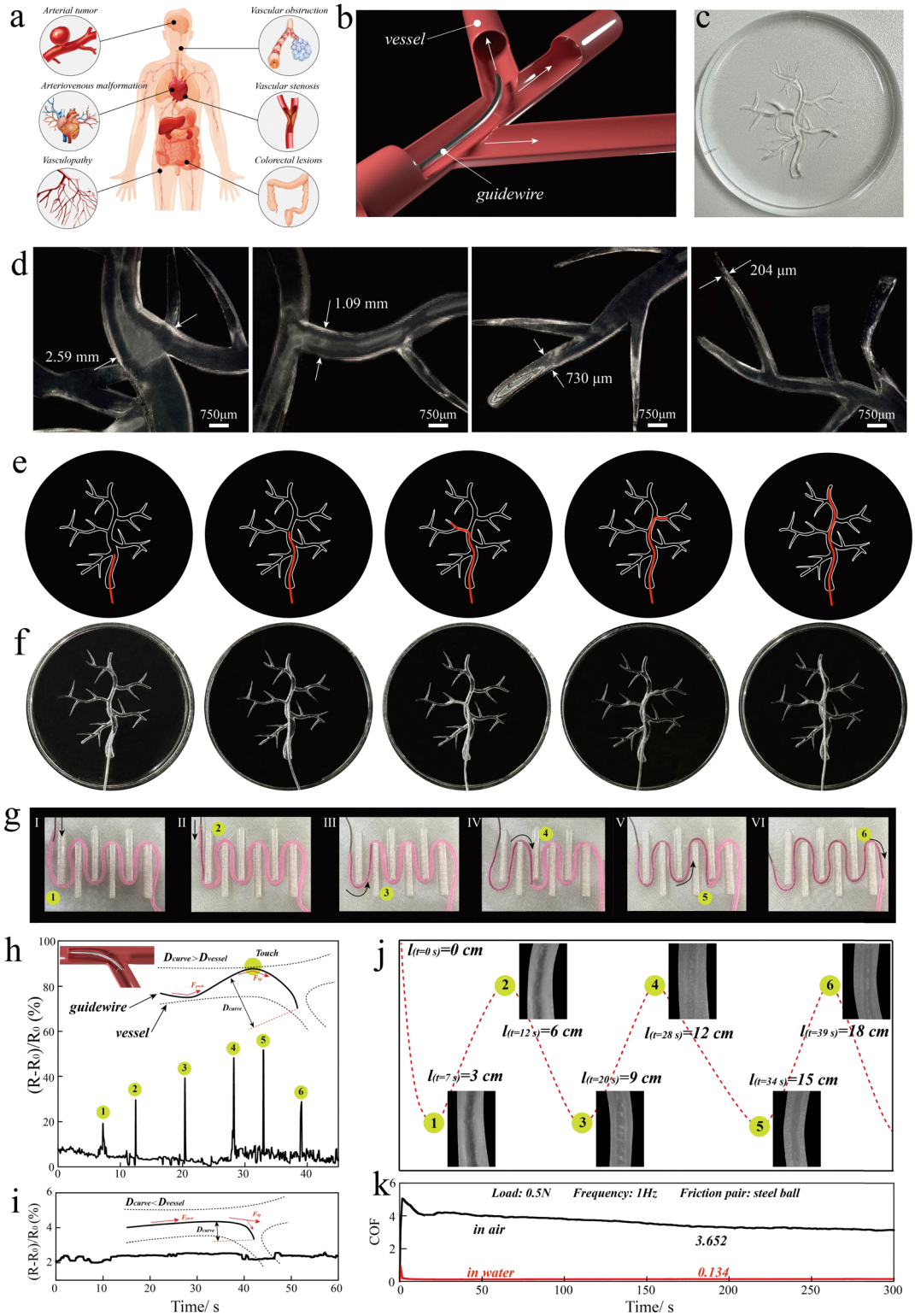

Fig. 5 Prepared vascular hydrogel models used for simulation of biomedical practices. (a) Different vessels in biological organs that can be fabricated by the AMA strategy. (b) Schematic illustration of the navigation of a medical guidewire within a vascular hydrogel model. (c) A photo of a 3D printed vascular hydrogel model with an internal interconnected structure. (d) Partially enlarged view of a tubular hydrogel architecture. Schematic diagram (e) and photos (f) of the guidewire navigation in vascular hydrogel models. (g) The guidewire navigation inside the serpentine tunnel-shaped hydrogel models with water as the lubricant. Green numbers represent the inflection point of the model. (h) The change in electrical signals generated at the inflection point due to the compression of the guidewire on the model wall. (i) No change of electrical signals generated without compression on the model wall. (j) The migration path curves and time of the guidewire within the channel of the hydrogel vessel. (k) Friction test curves of PVA–OH hydrogel tubes with or without water as the lubricant (load: 0.5 N, frequency: 1 Hz, and friction pair: steel ball).

interventions, replacing the need for human cadavers for ethical considerations. We try to demonstrate the vascular hydrogel model (adjusting the diameter according to different organs, Fig. 5a, the cell survival tests are shown in Fig. S11, ESI†) as the *in vitro* realistic hands-on platform for simulating the endovascular intervention (Fig. 5b and Fig. S12, ESI†). We fabricated a hydrogel model with sophisticated geometries and internally interconnected cavity architectures by imitating the complex structures of blood vessels (Fig. 5c). As can be seen from partially enlarged views in Fig. 5d, the diameters of cavity architectures range from 204 μm to 2.59 mm, almost covering the diameter range of blood vessels in the human body. Moreover, the exceptional lubricating properties of hydrogels enable smooth advancement of guidewires through the model vessels, reaching branched locations with ease and precision (Fig. 5e and f). Another example demonstrated real-time detection of the position of a guidewire in serpentine tunnel-shaped hydrogel models through changes in electrical signals (Fig. 5g). The hydrogel vascular model wall is compressed by the force of the guidewire movement, causing changes in the electrical signal that can accurately detect the guidewire's position in real-time. When the diameter of the curve exceeds that of the vessel, the electrical signal changes, as illustrated in Fig. 5h and i (the gauge factor (GF) is shown in Fig. S13, ESI†). This allows the guidewire to swiftly reach its intended location within the hydrogel vessel model, with monitoring facilitated through real-time signal alterations (Fig. 5j). The frictional characteristics of the inner surface are crucial for successful guidewire navigation. The inner surface of hydrogel models demonstrates a lower coefficient of friction and more consistent friction behavior, enabling efficient water lubrication during the guidewire navigation. Consequently, the sliding force experienced by the guidewire in hydrogel models is lower in water compared to that in air (Fig. 5k, schematic illustration of the friction process under different conditions shown in Fig. S13, ESI†). In summary, hydrogel vascular models can function as an *in vitro* platform for practicing hand–eye coordination in endovascular intervention simulations, owing to their softness, flexibility, wetness, lubrication, and tissue-matching mechanical properties.

3. Conclusion

In summary, inspired by the denaturing ability of spider silks, we have developed an innovative alkali-induced molecular aggregation (AMA) strategy to efficiently fabricate tubular hydrogel architectures with adjustable diameters. This strategy allows for the incorporation of 3D printing to rapidly produce biologically structured hydrogel models with interconnected vascular cavities, a feat that is challenging with other existing methods. The key to successful gelation lies in screening for suitable rheological properties and concentrations of the two solutions. The robust crosslink networks and adaptable 3D printing technology result in hydrogel vascular models with excellent mechanical properties and customizable diameters, thicknesses, and modulus. This novel approach offers an efficient and rapid method for fabricating hydrogel vascular models that could serve as a platform for testing new biomedical devices and techniques *in vitro*.

Data availability

The data used to support the findings of this study are available from the corresponding author upon request.

Conflicts of interest

We declare that we do not have any commercial or associative interest that represents a conflict of interest in connection with the work submitted.

Acknowledgements

This work was supported by the National Key R&D Program of China (2022YFB4600102), the Strategic Priority Program of the Chinese Academy of Sciences (XDB0470303), the National Natural Science Foundation of China (52175201, 51935012 and 52305229), the Research Program of Science and Technology Department of Gansu Province (22JR5RA107, 24JRRA044 and 22JR5RA093), the Major Program (ZYFZFX-2) and the Cooperation Foundation for Young Scholars (HZJJ23-02) of the Lanzhou Institute of Chemical Physics, CAS, the Shandong Provincial Natural Science Foundation (ZR2023QE090), the Taishan Scholars Program, and the Oasis Scholar of Shihezi University.

References

1 Lin Du, Chen Qin and Hongjian Zhang, *et al.*, Multicellular Bioprinting of Biomimetic Inks for Tendon-to-Bone Regeneration, *Adv. Sci.*, 2023, **10**(21), 01309.
2 Jay M. Taylor, Haiwen Luan and Jennifer A. Lewis, *et al.*, Biomimetic and Biologically Compliant Soft Architectures via 3D and 4D Assembly Methods: A Perspective, *Adv. Mater.*, 2022, **34**(16), 08391.
3 Pengju Li, Saehyun Kim and Bozhi Tian, Nanoenabled Trainable Systems: From Biointerfaces to Biomimetics, *ACS Nano*, 2022, **16**(12), 19651–19664.
4 Yawen Liu, Yushu Li and Qiyue Wang, *et al.*, Biomimetic Silk Architectures Outperform Animal Horns in Strength and Toughness, *Adv. Sci.*, 2023, **10**(29), 03058.
5 Junqi Yi and Xiaodong Chen, Polymer Films Inspired by Spider Silk Connect Biological Tissues and Electronic Devices, *Nature*, 2023, **624**, 295–302.
6 Daeshik Kang, Peter V. Pikhitsa and Yong Whan Choi, *et al.*, Ultrasensitive Mechanical Crack-based Sensor Inspired by the Spider Sensory System, *Nature*, 2014, **516**(7530), 222–226.
7 Wenhao Hou, Jiao Wang and Jiuan Lv, Bioinspired Liquid Crystalline Spinning Enables Scalable Fabrication of

High-Performing Fibrous Artificial Muscles, *Adv. Mater.*, 2023, **35**(16), 11800.
8 Gary J. Dunderdale, Sarah J. Davidson and Anthony J. Ryan, *et al.*, Flow-induced Crystallisation of Polymers from Aqueous Solution, *Nat. Commun.*, 2020, **11**(1), 3372.
9 Xin Chen, Zhengzhong Shao and David P. Knight, *et al.*, Conformation Transition Kinetics of Bombyx Mori Silk Protein, *Proteins: Struct., Funct., Bioinf.*, 2007, **68**(1), 223–231.
10 David Porter and Fritz Vollrath, Water Mediated Proton Hopping Empowers Proteins, *Soft Mater.*, 2013, **9**(3), 643–646.
11 Dapeng Bi, Jie Zhang and Bulbul Chakraborty, *et al.*, Jamming by Shear, *Nature*, 2011, **14**(480), 355–358.
12 Kenneth S. Schweizer and Galina Yatsenko, Collisions, Caging, Thermodynamics, and Jamming in the Barrier Hopping Theory of Glassy Hard Sphere Fluids, *J. Chem. Phys.*, 2007, **127**(16), 164505.
13 Qiguang He, Zhijian Wang and Yang Wang, *et al.*, Electrically controlled liquid crystal elastomer–based soft tubular actuator with multimodal actuation, *Sci. Adv.*, 2019, **5**, eaax5746.
14 Mengyuan Yang, Yiyi Xu and Xuan Zhang, *et al.*, Bioinspired Phototropic MXene-Reinforced Soft Tubular Actuators for Omnidirectional Light-Tracking and Adaptive Photovoltaics, *Adv. Funct. Mater.*, 2022, **32**, 2201884.
15 Qing Gao, Yong He and Jianzhong Fu, *et al.*, Coaxial Nozzle-assisted 3D Bioprinting with Built-in microchannels for Nutrients Delivery, *Biomaterials*, 2015, **61**, 203–215.
16 Ankit Gargava, Sohyun Ahn and William E. Bentley, *et al.*, Rapid Electroformation of Biopolymer Gels in Prescribed Shapes and Patterns: A Simpler Alternative to 3-D Printing, *ACS Appl. Mater. Interfaces*, 2019, **11**(40), 37103–37111.
17 Luiz E. Bertassoni, Martina Cecconi and Vijayan Manoharan, *et al.*, Hydrogel bioprinted microchannel networks for vascularization of tissue engineering constructs, *Lab Chip*, 2014, **14**(13), 2202–2211.
18 Benjamin Holmes, Kartik Bulusu and Michael Plesniak, *et al.*, A synergistic approach to the design, fabrication and evaluation of 3D printed micro and nano featured scaffolds for vascularized bone tissue repair, *Nanotechnology*, 2016, **27**(6), 064001.
19 Qingmegn Pi, Maharjan Sushila and Xiang Yan, *et al.*, Digitally Tunable Microfluidic Bioprinting of Multilayered Cannular Tissues, *Adv. Mater.*, 2018, **30**(43), 1706913.
20 Liucheng Zhang, Yi Xiang and Hongbo Zhang, *et al.*, A Biomimetic 3D-Self-Forming Approach for Microvascular Scaffolds, *Adv. Sci.*, 2020, **7**(9), 1903553.
21 Hyo-Ryoung Lim, Hee Seok Kim and Raza Qazi, *et al.*, Advanced Soft Materials, Sensor Integrations, and Applications of Wearable Flexible Hybrid Electronics in Healthcare, Energy, and Environment, *Adv. Mater.*, 2020, **32**, 1901924.
22 Yanzhao Yang, Xuan Zhang and Cristian Valenzuela, *et al.*, High-throughput printing of customized structural-color graphics with circularly polarized reflection and mechanochromic response, *Matter*, 2024, **7**(6), 2091–2107.
23 Yaxin Zhang, Fang Huang and Ercong Zhang, *et al.*, Effect of the Support Bath on Embedded 3D Printing of Soft Elastomeric Composites, *Mater. Lett.*, 2023, **331**, 133475.
24 Taylor E. Greenwood, Serah E. Hatch and Mark B. Colton, *et al.*, 3D Printing Low-stiffness Silicone within a Curable Support Matrix, *Addit. Manuf.*, 2021, **37**, 101681.
25 Joseph T. Muth, Daniel M. Vogt and Ryan L. Truby, *et al.*, Embedded 3D Printing of Strain Sensors within Highly Stretchable Elastomers, *Adv. Mater.*, 2014, **26**(36), 6307–6312.
26 Ziqi Gao, Jun Yin and Peng Liu, *et al.*, Simultaneous Multimaterial Embedded Printing for 3D Heterogeneous Structures, *Int. J. Extreme Manuf.*, 2023, **5**(3), 035001.
27 Shaoxing Qu, 3D printing of hydrogel electronics, *Nat. Electron.*, 2022, **5**, 838–839.
28 Doruk Erdem Yunus, Salman Sohrabi and Ran He, *et al.*, Acoustic Patterning for 3D Embedded Electrically Conductive Wire in Stereolithography, *J. Micromech. Microeng.*, 2017, **27**(4), 045016.
29 Liqun Ning, Riya Mehta and Cong Cao, *et al.*, Embedded 3D Bioprinting of Gelatin Methacryloyl-Based Constructs with Highly Tunable Structural Fidelity, *ACS Appl. Mater. Interfaces*, 2020, **12**(40), 44563–44577.
30 Maria Stang, Joshua Tashman and Daniel Shiwarski, *et al.*, Embedded 3D Printing of Thermally-Cured Thermoset Elastomers and the Interdependence of Rheology and Machine Pathing, *Adv. Mater. Technol.*, 2022, **8**(3), 00984.
31 Qian Wu, Kaidong Song and Deming Zhang, *et al.*, Embedded Extrusion Printing in Yield-stress-fluid Baths, *Matter*, 2022, **5**(11), 3775–3806.
32 Bhattacharjee Tapomoy, Zehnder M. Steven and Rowe G. Kyle, *et al.*, Writing in the Granular Gel Medium, *Sci. Adv.*, 2015, **1**(8), 1500655.
33 Corwin I. Eric, Jaeger M. Heinrich and Nagel R. Sidney, Structural Signature of Jamming in Granular Media, *Nature*, 2005, **435**, 1075–1078.
34 Jiang Pan, Zhongying Ji and Desheng Liu, *et al.*, Growing Hydrogel Organ Mannequins with Interconnected Cavity Structures, *Adv. Funct. Mater.*, 2022, **32**(13), 08845.
35 Yang Lyu, Rui Guo and Zhengwei Lin, *et al.*, Ion Clusters-Driven Strong and Acid/Alkali/Freezing-Tolerant Conductive Hydrogels for Flexible Sensors in Extreme Environments, *Adv. Funct. Mater.*, 2023, **33**(50), 2306300.
36 Jiatian Li, Sitong Li and Jiayi Huang, *et al.*, Spider Silk-Inspired Artificial Fibers, *Adv. Sci.*, 2022, **9**(5), 2103965.
37 Aniela Heidebrecht, Lukas Eisoldt and Johannes Diehl, *et al.*, Biomimetic Fibers Made of Recombinant Spidroins with the Same Toughness as Natural Spider Silk, *Adv. Mater.*, 2015, **27**(13), 2189–2194.
38 Marlene Andersson, Qiupin Jia and Ana Abella, *et al.*, Biomimetic Spinning of Artificial Spider Silk from a Chimeric Minispidroin, *Nat. Chem. Biol.*, 2017, **13**(3), 262–264.
39 Yuchao Wu, Darshi U. Shah and Baoyuan Wang, *et al.*, Biomimetic Supramolecular Fibers Exhibit Water-Induced Supercontraction, *Adv. Mater.*, 2018, **30**(27), 1707169.
40 Mohammad Ali Darabi, Ali Khosrozadeh and Ying Wang, *et al.*, An Alkaline Based Method for Generating Crystalline,

Strong, and Shape Memory Polyvinyl Alcohol, *Biomaterials*, 2020, **7**, 1901740.

41 Edmund M. Choy, D. Fennell Evans and E. L. Cussler, Selective Membrane for Transporting Sodium Ion Against its Concentration Gradient, *J. Am. Chem. Soc.*, 1974, **96**(22), 7085–7090.

42 Zainab Waheed Abdullah, Yu Dong and Jeffery Ian Davies, *et al.*, PVA, PVA Blends, and Their Nanocomposites for Biodegradable Packaging Application, *Polym.-Plast. Technol. Eng.*, 2017, **56**(12), 1307–1344.

43 Jinbiao Min, Zhaoxi Zhou and Jia Zheng, *et al.*, Self-Healing, Water-Retaining, Antifreeze, Conductive PVA/PAA-PAM-IS/GC Composite Hydrogels for Strain and Temperature Sensors, *Macromol. Mater. Eng.*, 2022, **307**(7), 2100948.

44 Ying Zhu, Youhong Guo and Kaiyue Cao, *et al.*, A general strategy for synthesizing biomacromolecular ionogel membranes via solvent-induced self-assembly, *Nat. Synth.*, 2023, **2**, 864–872.

45 Qiang Zou, Shiwen Zhang and Qi Su, *et al.*, Flexible Multimodal Sensor Based on Double-network Hydrogel for Human and Robotic Applications, *ChemistrySelect*, 2023, **8**(11), e202204319.

46 Xiaoyan Hong, Hao Ding and Jiao Li, *et al.*, Poly(acrylamide-*co*-acrylic acid)/chitosan Semi-Interpenetrating Hydrogel for Pressure Sensor and Controlled Drug Release, *Polym. Adv. Technol.*, 2021, **32**(8), 3050–3058.

47 Tingting Wang, Jinqing Wang and Zhangpeng Li, *et al.*, PVA/SA/MXene Dual-network Conductive Hydrogel for Wearable Sensor to Monitor Human Motions, *J. Appl. Polym. Sci.*, 2022, **139**(7), e51627.

48 Gang Ge, Yizhou Zhang and Jinjun Shao, *et al.*, Stretchable, Transparent, and Self-Patterned Hydrogel-Based Pressure Sensor for Human Motions Detection, *Adv. Funct. Mater.*, 2018, **28**(32), 1802576.

49 Jiayuan Ren, Yanhui Liu and Zengqiang Wang, *et al.*, An Anti-Swellable Hydrogel Strain Sensor for Underwater Motion Detection, *Adv. Funct. Mater.*, 2022, **32**(13), 2107404.

50 Meijin Zhao, Wenshuai Zhang and Dan Wang, *et al.*, A Packaged and Reusable Hydrogel Strain Sensor with Conformal Adhesion to Skin for Human Motions Monitoring, *Adv. Mater. Interfaces*, 2022, **9**(6), 2101786.

51 Dong Liu, Honghao Zhou and Yuanyuan Zhao, *et al.*, A Strand Entangled Supramolecular PANI/PAA Hydrogel Enabled Ultra-Stretchable Strain Sensor, *Small*, 2022, **18**(47), 2203258.

52 Yan Bai, Yuyuan Lu and Shuaihang Bi, *et al.*, Stretchable and Photothermal MXene/PAA Hydrogel in Strain Sensor for Wearable Human-Machine Interaction Electronics, *Adv. Mater. Technol.*, 2023, **8**(9), 2201767.

53 Lin Guan, Hou Liu and Xiaojun Ren, *et al.*, Balloon Inspired Conductive Hydrogel Strain Sensor for Reducing Radiation Damage in Peritumoral Organs During Brachytherapy, *Adv. Funct. Mater.*, 2022, **32**(22), 2112281.

54 Xudong Ma and Xieraili Maimaitiyiming, Highly Stretchable, Self-Healing, and Low Temperature Resistant Double Network Hydrogel Ionic Conductor as Flexible Sensor and Quasi-Solid Electrolyte, *Macromol. Rapid Commun.*, 2022, **44**(3), 2200685.

55 Tianyi Hang, Yiming Chen and Fuqiang Yin, *et al.*, Highly Stretchable Polyvinyl Alcohol Composite Conductive Hydrogel Sensors Reinforced by Cellulose Nanoffbrils and Liquid Metal for Information Transmission, *Int. J. Biol. Macromol.*, 2024, **258**, 128855.

56 Murphy V. Sean and Atala Anthony, 3D Bioprinting of Tissues and Organs, *Nat. Biotechnol.*, 2014, **32**, 773–785.

57 Willie Wu, Deconinck Adam and Lewis A. Jennifer, Omnidirectional Printing of 3D Microvascular Networks., *Adv. Mater.*, 2011, **23**, H178–H183.

